Mon. Not. R. Astron. Soc. **000**, 1–15 (2012) Printed 19 December 2012 (MN LATEX style file v2.2)

# Ellipsoidal halo finders and implications for models of triaxial halo formation

Giulia Despali[1⋆], Giuseppe Tormen[1], Ravi K. Sheth[2,3]

[1] *Dipartimento di Fisica e Astronomia, Università di Padova, vicolo dell'Osservatorio 3, 35122, Padova, Italy*
[2] *The Abdus Salam International Center for Theoretical Physics, Strada Costiera 11, 34151 Trieste, Italy*
[3] *Center for Particle Cosmology, University of Pennsylvania, 209 S 33rd St, Philadelphia, PA 19104, USA*

arXiv:1212.4157v1 [astro-ph.CO] 17 Dec 2012

**ABSTRACT**

We describe an algorithm for identifying ellipsoidal haloes in numerical simulations, and quantify how the resulting estimates of halo mass and shape differ with respect to spherical halo finders. Haloes become more prolate when fit with ellipsoids, the difference being most pronounced for the more aspherical objects. Although the ellipsoidal mass is systematically larger, this is typically by less than 10% for most of the haloes. However, even this small difference in mass corresponds to a significant difference in shape from the spherical counterpart. We quantify these effects on the initial mass and deformation tensors, on which most models of triaxial collapse are based.

By studying the properties of protohaloes in the initial conditions, we find that models in which protohaloes are identified in Lagrangian space by three positive eigenvalues of the deformation tensor are tenable only at the masses well-above $M_*$. The overdensity $\delta$ within almost any protohalo is larger than the critical value associated with spherical collapse; this is in good qualitative agreement with models which identify haloes requiring that collapse have occured along all three principal axes, each axis having turned around from the universal expansion at a different time. On average, $\delta$ increases as mass $M$ decreases, scaling as $\delta_c(1+0.2\sigma)$ with rms scatter $0.2\sigma(M)$. The mean ellipticity $e$ and prolateness $p$ of the deformation tensor both increase as $M$ decreases ($\langle e\delta/\sigma\rangle = 0.4$, $rms_e = 0.14$; $\langle p\delta/\sigma\rangle = 0$, $rms_p = 0.15$). These values are in good qualitative agreement with the simplest predictions associated with the ellipsoidal collapse model, if one assumes protohaloes were initially spherical, and they collapsed around random positions which were sufficiently overdense.

However, most protohaloes are not spherical and departures from sphericity increase as protohalo mass decreases. The mass and deformation tensors are well-aligned, in agreement with the fundamental assumption of the ellipsoidal collapse model, and with models which identify haloes with peaks in the initial density fluctuation field. But the direction of maximum initial compression coincides with the direction of what is initially the longest axis, contrary to what the peaks model predicts. By the final time, it is the shortest axis of the final object which tends to be aligned with the direction of initial maximal compression: the alignment changes during the evolution.

**Key words:** galaxies: clusters: general - cosmology: theory - dark matter

## 1 INTRODUCTION

In the standard cosmological model, the structures observed today are assumed to have grown gravitationally from small, initially Gaussian density fluctuations. Collapsed, virialized dark matter haloes form from the initial fluctuation field, leading to structure formation: as the universe expands, sufficiently overdense regions expand until they reach a maximum size, after which they collapse under the action of their own gravity. It is within these haloes that gas cools and stars are born. This process may be studied using both analytical models or numerical simulations, in order to understand just what it is that determines when and where an object will collapse (Lacey & Cole 1993, 1994; Kauffmann & White 1993; Springel et al. 2001b; Giocoli et al. 2007).

In the Spherical Collapse model (hereafter SC) (Gunn 1977), which describes the evolution of a spherical mass shell within an expanding background, the entire evolution is de-

⋆ E-mail: giulia.despali@studenti.unipd.it

termined by the initial overdensity within the protohalo. In this model, the initially spherical region remains spherical – only its size changes – and there is a critical initial overdensity $\delta_{sc}$ which a proto-halo must have for it to collapse and virialize by a given time (e.g. the present). Moreover, this value is the same for all haloes, whatever their mass.

The next more complicated model assumes an Ellipsoidal Collapse (hereafter EC) (White & Silk (1979), Bond & Myers (1996)). In the formulation of Bond & Myers (1996), the triaxiality in the potential leads to tidal forces which deform the shape of the object as it evolves. Hence, even if the mass distribution of the protohalo was initially spherical, the final virialized object need not be a sphere. Most implementations of the EC model have assumed initially spherical shapes (Sheth et al. 2001; Sheth & Tormen 2002; Desjacques 2008; Lam & Sheth 2008; Rossi et al. 2011), though this is not a fundamental assumption (Shen et al. 2006). Since the EC model generically predicts non-spherical shapes for virialized objects, and simulated haloes are well-known to be triaxial (Jing & Suto 2002; Allgood et al. 2006), the EC model is widely expected to be more realistic than the SC model.

Despite this, simulated haloes are often still identified by searching for a critical overdensity within a sphere, or deforming such a candidate spherical region along its principal axes. Therefore, one of the goals of this paper is to present a method for identifying ellipsoidal haloes which we believe provides a more accurate estimate of halo masses and shapes. We then explore how our new method impacts estimates of the resulting halo properties (e.g. mass, shape) at the present time, and in the initial conditions (e.g., mass and deformation tensors of the proto-halo). We believe the latter allows for more direct and quantitative tests of the EC model.

The outline of this paper is as follows. In Section 2 we highlight those aspects of the Ellipsoidal Collapse model which are most relevant to our study. Section 3 describes our dataset and the halo identification algorithm, explaining how we improve our estimates of halo shapes, by defining them as virialized ellipsoids rather than spheres. In Section 4 we present our results concerning the difference in mass (Subsection 4.1) and in final shape (4.2) with respect to the usual spherical one. In Section 5 we study the initial density fluctuation field of the proto-haloes, showing how the difference between the two methods is reflected in the initial properties of the haloes (Subsection 5.1); and how the initial properties influence the subsequent evolution (5.2). In Section 6 we discuss the average evolution of halo shape and orientation. A few case-by-case examples are presented in an Appendix. We summarize and discuss our results and then conclude in Section 7.

## 2 THE ELLIPSOIDAL COLLAPSE MODEL

Many of the quantities we measure in the simulations are motivated by our desire to test various assumptions of the EC model. So it is useful to summarize these here.

### 2.1 Does only potential matter?

Although the EC model of Bond & Myers (1996) does not require it, all implementations of it assume that the mass distribution of a proto-halo is initially spherical. In this case, the evolution of the shape is determined by just three numbers, which are specific combinations of the three eigenvalues of the initial $3 \times 3$ deformation tensor centered on the center of mass of the proto-halo. (Strictly speaking the tensor is evaluated after smoothing the initial fluctuation field on the scale which contains all the mass which will end up in the halo.) Because the shape of the object is determined by the initial deformation tensor, in this model, the mass and deformation tensors are perfectly aligned *by definition*. Measurements in simulations have shown that this vast simplification is actually a rather good approximation (Porciani et al. 2002). This means that tidal torques, induced by the misalignment between these tensors, are subdominant.

Therefore, in this model, the proto-halo shrinks (in comoving coordinates) fastest along the axis corresponding to the direction of maximum compression, forming a pancake; this is followed by collapse along the second and then finally along the axis of least compression eventually resulting in a virialized object. I.e., the three axes collapse at different times, which depend on the local shape of the deformation tensor, but because the initial shape of the mass tensor was spherical, the ordering of the axis lengths is monotonic in time, and collapse times are determined by the initial compression factors: larger compression factor means earlier collapse.

A final assumption of the model is that virialization corresponds to collapse along all three axes. Since the first axis to collapse and freeze-out from the expansion of the background Universe will have done so when the universe was denser, this first axis to collapse will also be the shortest axis of the virialized object, and the third will be longest. I.e., the shortest axis at virialization will be aligned with the direction of initial maximum compression, and vice versa.

The three numbers which determine the evolution in this model are the initial density contrast $\delta_i$ (the only number that matters for the spherical evolution model), and the ellipticity and prolateness parameters $e$ and $p$ of the deformation tensor (i.e. not the mass tensor). These are defined as follows. If the eigenvalues of the deformation tensor are $\lambda_1 \geqslant \lambda_2 \geqslant \lambda_3$, then

$$\delta_i \simeq \lambda_1(t_i) + \lambda_2(t_i) + \lambda_3(t_i) \tag{1}$$

and

$$e = \frac{\lambda_1(t_i) - \lambda_3(t_i)}{2\delta(t_i)} \qquad \text{and} \qquad p = \frac{\lambda_1(t_i) + \lambda_3(t_i) - 2\lambda_2(t_i)}{2\delta(t_i)} \tag{2}$$

where $e \geqslant 0$ and $|p| \leqslant e$; a sphere has $e = p = 0$, prolate configurations have $-e \leqslant p \leqslant 0$, and $0 \leqslant p \leqslant e$ are oblate.

Sheth et al. (2001) showed that, in this model

$$\frac{\delta_{ec}(e,p)}{\delta_{sc}} = 1 + \beta \left[ 5(e^2 \pm p^2) \frac{\delta_{ec}^2(e,p)}{\delta_{sc}^2} \right]^{\gamma}, \tag{3}$$

where $\beta = 0.47$ and $\gamma = 0.615$. Note that non-spherical effects always make $\delta_{ec}(e,p) > \delta_{sc}$, a point to which we will return. Sheth et al. (2001) also showed that, in a Gaussian random fluctuation field, $\delta, e, p$ can vary from one position to another, with the consequence that even at fixed mass,

$\delta_{ec}$ can vary from one proto-halo to another. They then used the statistics of Gaussian fields to argue that, on average, $\delta_{ec}$ will be close to $\delta_{sc}$ at large masses, but it will increase as mass decreases. They showed that this mass dependence of $\delta_{ec}$ was indeed evident in their simulations, and so it is now commonly assumed that the EC model describes some of the physics which is relevant to the triaxial shapes of virialized haloes in simulations. In what follows, we test this in slightly more detail by checking if the dependence on $e$ and $p$ is as predicted.

### 2.2 What if the initial shape is not spherical?

However, we already know that there is one respect in which the EC model fails. This is because the model predicts that the large proto-halo patches which collapse to form massive haloes should be more spherical. Therefore, the shape at virialization should also be more spherical (Rossi et al. 2011). Simulations show that, in fact, the most massive virialized haloes can be quite triaxial (Jing & Suto 2002; Allgood et al. 2006). This raises the question of whether the EC model has failed to identify the correct shapes in the initial conditions, or if its approximation of the evolution is incorrect.

For example, the next simplest model would begin with proto-haloes with triaxial rather than spherical mass distributions, but will keep the assumption that the mass and deformation tensors are perfectly aligned. In this case, the evolution of the shape, and hence the time required to collapse and virialize depends on $\delta, e, p$ as well as on the initial axis lengths (i.e., the square-roots of the eigenvalues of the mass tensor), and on whether or not the direction of maximum compression is oriented along the initially longest or the shortest axis. In such a model, one might postulate for example that haloes form at those special points in space where all three axes would have turned around or collapsed at the same time; this would happen if the axis which was initially the longest also had the largest compression factor initially ('perfect' alignment). This correlation between the directions of the longest initial axis and the largest compression factor is indeed seen in simulations (Porciani et al. 2002), in the sense that $\cos\theta_{11} \sim 1$ where $\theta_{11}$ is the angle between these two vectors.

In fact, despite the theoretical simplicity of these 'perfect' alignment models , the evolution of the shape can appear to be more complex because, e.g., if the axis that was longest initially also had the largest compression factor, then it may eventually become shorter than what was initially the second longest axis. So one might ask, even though the shortest axis initially may not be the shortest finally, is it still true that the shortest axis at virialization tends to be aligned with the direction of initial maximum compression (and vice versa)? If it does, then this would still be in agreement with an EC model for the evolution, only applied to a non-spherical initial mass distribution.

The Zel'dovich approximation (Zel'dovich 1970), provides an easy way to see the qualitative features discussed above. In this case, the eigenvalues are assumed to evolve as $\lambda_j(t) = \lambda_j(t_i)\, D(t)/D(t_i)$, where $D(t)$ is the linear theory growth factor at time $t$. This means that the comoving axis lengths evolve independently of one another, as $R_j(t) = R_j(t_i)[1 - \lambda_j(t)]$. Notice that in this approximation a positive eigenvalue implies contraction, whereas a negative eigenvalue implies expansion.

The nonlinear density is the ratio of the mass of the proto-halo to its volume. Mass conservation means that it satisfies

$$1 + \delta(t) = \frac{M}{\bar{\rho} V(t)} = \frac{1}{\prod_{j=1}^{3} 1 - \lambda_j(t)}. \qquad (4)$$

Notice that this expression applies even if the $R_j(t_i)$ are not equal; it reduces to $\delta_i = \sum_{j=1}^{3} \lambda_j$ for very small values of $\lambda_i$.

In this approximation the collapse of axis $j$ corresponds to the time when $1-\lambda_j(t) = 0$. When the $R_j(t_i)$ are all equal, then the order of the axis lengths $R_j$ at any given time is determined completely by the ordering of the $\lambda_j$ at the initial time. But if they are not equal, then, although the order of the time to complete collapse is still determined by the order of the $\lambda_j$, the axis lengths at some time prior to complete collapse may not. E.g., if $R_j > R_k$ *and* $\lambda_j > \lambda_k$ then $R_j$ must collapse before $R_k$, so at some point it must become smaller than $R_k$. Notice that, despite this reordering of the axis lengths, the three fundamental directions of the principal axes of the mass tensor will *not* have changed. Of course, this means that if one studies the direction in which 'the longest axis' points, then this direction may change suddenly (e.g., at the time when it stops being the longest).

Although Shen et al. (2006) provide a simple approximation to the evolution predicted by the EC model when the initial shape is not a sphere, which can be thought of as a simple physically motivated modification to the Zeldovich approximation, we believe that a complete understanding of these and related aspects of the EC model is still missing. For example, we noted that $\cos\theta_{11} \sim 1$, where $\theta_{11}$ is the angle between the longest axis and the direction of maximum compression. While we confirm that $\cos\theta_{11} \sim 1$, the torque generated by the misalignment between these two vectors depends on $\sin\theta_{11}$, and it can be quite different from zero even though $\cos\theta \sim 1$ (basically because $\cos 30^\circ \sim 0.866$ but $\sin 30^\circ \sim 0.5$). Thus, even a small misalignment can have a dramatic effect, so further study of slightly misaligned models is certainly needed.

Even so, a comparison between simplified models such as these and simulations clearly depends critically on correctly identifying the proto-haloes in the initial conditions, and this in turn depends on identifying the particles which belong to the final virialized haloes. Therefore, in what follows, we analyse in detail the shapes of haloes, how these depend on the method of estimation, how they evolve, and how this evolution is influenced by the potential field.

## 3 SIMULATION DATA

We address these questions by studying the properties of haloes identified in the GIF2 simulation.

### 3.1 The GIF2 simulation

The GIF2 Simulation (Gao et al. 2004) adopts a ΛCDM cosmological model with $\Omega_m = 0.3$, $\Omega_\Lambda = 0.7$, $\sigma_8 = 0.9$ and $h = 0.7$. It follows $400^3$ particles in a periodic cube of side $110h^{-1}$ Mpc from an initial redshift $z = 49$ to the present

time. The associated change in the linear theory growth factor is $D_+(z=0)/D_+(z=49) = 38.993$. The individual particle mass is $1.73 \times 10^9 h^{-1}\ M_\odot$. Initial conditions were produced by imposing perturbations on an initially uniform state represented by a glass distribution of particles (White 1996); based on the Zel'dovich approximation (Zel'dovich 1970), a Gaussian random field is set up by perturbing the positions of the particles and assigning them velocities according to the growing model solution of linear theory (Seljak & Zaldarriaga 1996). The critical value of the linear theory overdensity that is required for spherical collapse at the present time is $\delta_c = 1.6755$.

### 3.2 Halo identification

Dark matter haloes are identified as local maxima in the density field: this is commonly done by growing spherical shells around the halo center - defined for example by the position of its most bound particles - and finding some characteristic radius $R$ where the mass overdensity reaches a given value: $\delta_{vir} \equiv (\rho(<R) - \rho_b)/\rho_b$, with $\rho_b$ the mean density of the universe and $\rho(<R)$ the average density inside radius $R$. Common choices for this *virial* overdensity are 200 times the background density, 200 times the critical density, and the value prescribed by the spherical collapse model: $\delta_{vir} = 323.7$ (at $z = 0$ for the assumed cosmological model - Eke et al. (1996)); this algorithm is known as Spherical Overdensity (SO).

Another method for identifying collapsed structures uses a percolation algorithm, called Friends of Friends (FOF), that links together particles closer than $bd$, where $d$ is the mean interparticle separation and $b < 1$ is called *linking length*; $b = 0.2$ is a common choice, as it identifies structures with average density of order one hundred times ($\sim 1/5^3\times$) the background. *FOF* haloes are usually not spherical, but closely follow the isodensity contours of the identified structures, giving a more realistic representation of the halo shape. On the other hand, this algorithm may link together haloes which are dynamically different, if particle noise is such that there exists a thin bridge of particles connecting them.

A third and far less commonly used option is to define haloes as triaxial ellipsoids, as we do in the present work. Specifically, we will define haloes as triaxial structures with mean overdensity $\delta = \delta_{vir}$. Although computationally more costly, this method tries to retain the advantages of both previous ones: a theoretically motivated virial overdensity value and a more realistic description of the actual halo shape. This description is more consistent with the EC model, which naturally predicts triaxial rather than spherical haloes. In the next Subsection we will describe our algorithm in detail.

### 3.3 Triaxial haloes

The volume $V$ of a triaxial ellipsoid is defined by $V = (4\pi/3)abc$, with $a, b$, and $c$ the longest, intermediate and shortest axis, respectively. In order to find the ellipsoidal shape which best fits a given halo, we first run an *SO* algorithm on the full simulation and find for each halo its virial radius $R_V$, enclosing an average overdensity $\delta_{vir}$ (Tormen et al. 2004; Giocoli et al. 2008). We then calculate the mass tensor $M_{\alpha\beta}$ defined by the $N_V$ particles found inside $R_V$ as:

$$M_{\alpha\beta} = \frac{1}{N_V}\sum_{i=1}^{N_V} r_{i,\alpha} r_{i,\beta} \tag{5}$$

where $\mathbf{r}_i$ is the position vector of the $i$th particle and $\alpha$ and $\beta$ are the tensor indices. Note that, even if the halo distribution can be recovered from both, this is different from the inertia tensor which is defined as:

$$I_{\alpha\beta} = \sum_{i=1}^{N} m_i(\mathbf{r}_i^2\delta_{\alpha\beta} - r_{i,\alpha} r_{i,\beta}). \tag{6}$$

As explained in Bett et al. (2007), much of the literature confuses the two tensors and uses both interchangeably to describe the mass distribution.

The mass tensor so found will not be isotropic even for particles within a sphere if the particle distribution inside $R_V$ is not isotropic. Therefore, by diagonalizing $M_{\alpha\beta}$ we will obtain eigenvalues and eigenvectors which give an initial guess for the true shape and orientation of the virialized structure: the axes of the best fitting ellipsoid are defined as the square roots of the mass tensor eigenvalues. We then modify the list of particles which make up the halo by performing a sort of *Ellipsoidal Overdensity* criterion: for each particle selected in the previous step, we calculate its ellipsoidal distance from the center as

$$r_E^3 = \frac{\Delta x^2}{l_1^2} + \frac{\Delta y^2}{l_2^2} + \frac{\Delta z^2}{l_3^2}, \tag{7}$$

where $l_1^2$, $l_2^2$ and $l_3^2$ are the eigenvalues of the mass tensor calculated at the previous step. (The eigenvalues of the inertia tensor would be $l_2^2 + l_3^2$, $l_1^2 + l_3^2$ and $l_1^2 + l_2^2$.) Sorting the particles by ellipsoidal distance from the center of the halo, we build up an ellipsoid which encloses an average overdensity $\delta_{vir}$. We believe that using the overdensity to select the halo particles is more precise and consistent than requiring the volume of the ellipsoid equal that of the original SO sphere, or requiring the longest axis equal that of the initial sphere (Warren et al. 1992; Allgood et al. 2006; Schneider et al. 2012). This also allows a more direct comparison with theoretical models. We recalculate the mass tensor for this new particle distribution, and obtain a new set of eigenvectors, which improve the previous description of the halo shape. We iterate this calculation until the algorithm converges to a set of eigenvectors to better than one percent in the axial ratios. The final result is a new halo catalogue which is the one we study in the remainder of this work.

## 4 HALOES AT $Z = 0$

Figure 1 illustrates the difference between a spherical halo and its triaxial counterpart: black dots show the projected distributions of halo particles inside the final ellipsoid, while the red dashed circle indicates the virial radius $R_V$. The triaxial shape is more elongated when measured inside an ellipsoidal volume (in this case particularly in the $y$-$z$ plane) and follows the natural orientation of the halo and its isodensity contours more accurately than does the *SO* halo. We expect, therefore, an increase in virial mass $M$: this is true for the test halo of Figure 1 and in the next Section we will show results for the whole halo sample.

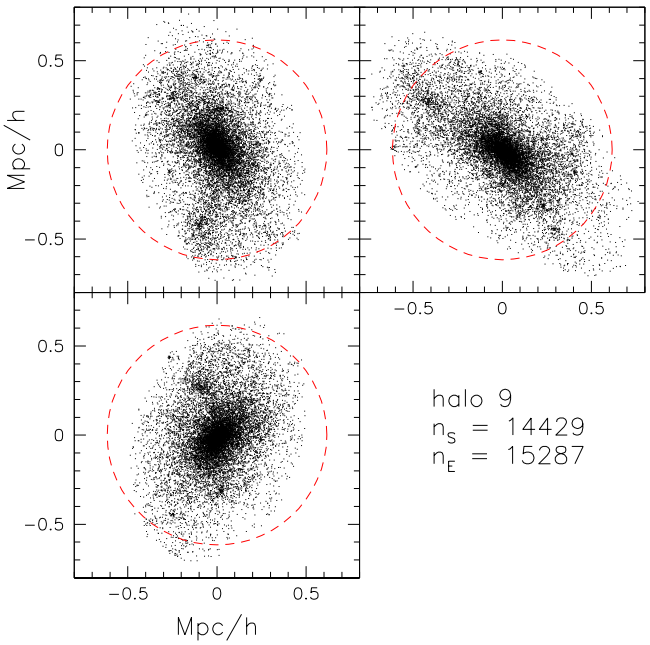


**Figure 1.** Example of the difference between the final ($z = 0$) spherical or ellipsoidal identification for a halo of the simulation: we show the projected distribution (in the $x$-$y$, $y$-$z$, $x$-$z$ planes) of the halo particles inside the ellipsoid; the red dashed circle indicates the radius of the halo in the spherical identification. We note that the shape becomes in general more elongated and that the number of particles increases, indicating that the ellipsoidal shape traces the isodensity contours better than the spherical one.

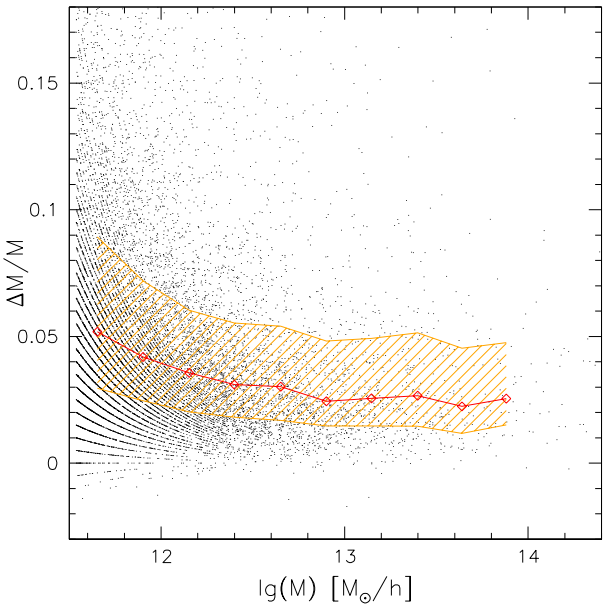


**Figure 2.** The mass difference between the ellipsoidal and spherical identification methods, shown as a function of the spherical mass. The medians of the distribution are shown in red and the region which lies between the first and third quartiles is shaded orange.

### 4.1 Difference in mass

In Figure 2 we plot the fractional difference in mass between the ellipsoidal and spherical identifications, defined by the ratio

$$\frac{\Delta M}{M} = \frac{M_E - M_S}{M_S} \tag{8}$$

as a function of the spherical mass $M_S$. Notice that our new method indeed gives a different estimate of the mass: at low masses the median difference of about 5% is larger than at high masses. This indicates that small mass haloes are more elongated and so the SO estimate is more biased than it is at larger masses. The ellipsoidal mass is clearly larger than the spherical one, as ellipsoids indeed trace the isodensity surfaces more precisely, and so include more particles. Of course the difference between the two estimates cannot be too big, since the ellipsoidal mass is a refinement of the spherical one. This has a positive implication: the spherical overdensity criterion, which is simpler than our best fitting ellipsoid method and requires fewer calculations, turns out to be quite precise in estimating the halo mass and thus the halo mass function. However, as we will show in the next section, the ellipsoidal description is much more appropriate for estimating halo shapes. There is a small fraction of haloes (less than 1%) which have negative values of $\Delta M/M$: by individual inspection, we found that they all correspond to merging haloes. Moreover, the initial (Lagrangian space) distribution of their particles is often fragmented in two or more large regions. We exclude them from further analysis.

### 4.2 Difference in final shape

We now study halo shapes. Figure 3 shows the fractional difference in the axial ratios $c/a$ and $b/a$ (with $a \geqslant b \geqslant c$), as a function of the spherical axial ratios using the fractional differences

$$\frac{\Delta(c/a)}{(c/a)_S} = \frac{(c/a)_E - (c/a)_S}{(c/a)_S} \tag{9}$$

and similarly for $b/a$. Ellipsoidal haloes are, of course, more ellipsoidal, so $\Delta(c/a)/(c/a), \Delta(b/a)/(b/a) \leqslant 1$ . When the axial ratio approaches 1, then haloes are almost spherical, so the ellipsoidal method correctly returns a spherical shape. The difference increases as $(c/a)_S$ and $(b/a)_S$ decrease: in particular, ellipsoidal-based shapes become more prolate, since the shortest axis changes more than the others, as can be seen by comparing the two panels of Figure 4. This agrees with the recognised preference for prolate halo shapes in previous works.

In Figure 4 we show the differential and cumulative distributions for both $c/a$ and $b/a$: the distribution obtained using final spheres is represented by the solid line, while the dashed line is for ellipsoids. There are more objects with small $c/a$ when fitting ellipsoids, and the median is shifted to smaller values. This is also true for the $b/a$ distribution, although the differences are smaller, implying a preference for more prolate shapes. This confirms what we already noticed in Figure 3. A similar result was obtained by Warren et al. (1992), who compared the axial ratios of a spherical and an ellipsoidal halo, finding a change in the axial ratios in the direction of a more ellipsoidal shape.

It is also interesting to study the halo structure at a

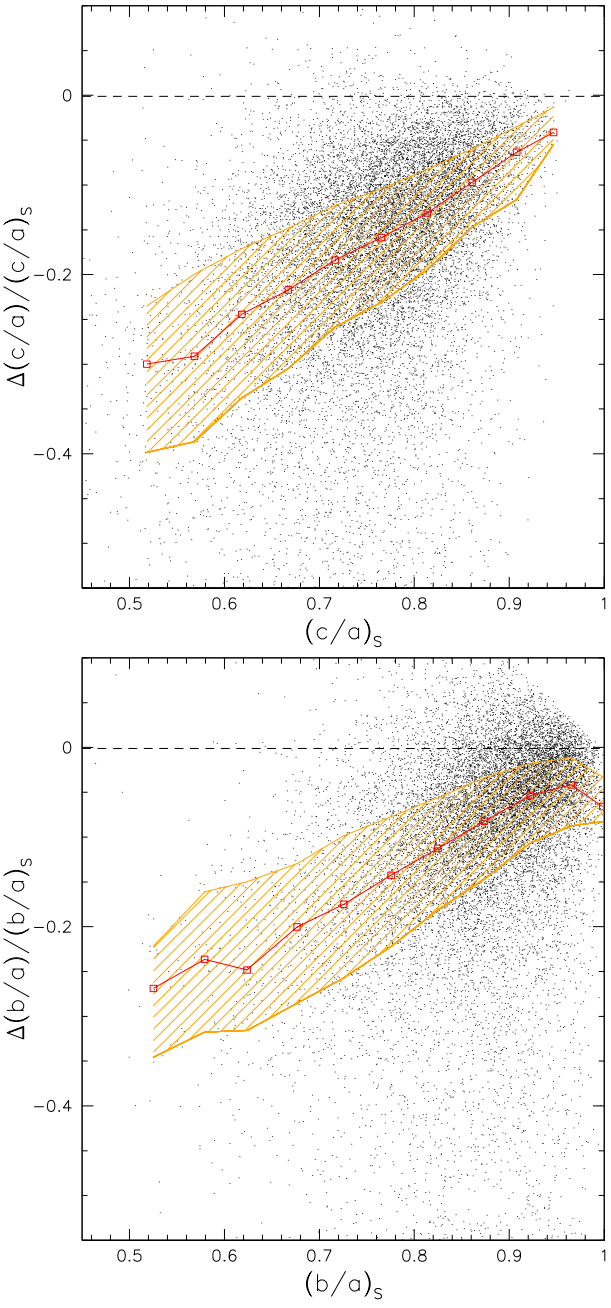


**Figure 3.** The difference in the final axial ratios $c/a$ and $b/a$ ($a \leqslant b \leqslant c$), as a function of the spherical ones. The orange shaded region lies between the first and third quartiles; red points show the median. The relative difference is generally negative, indicating that fitting ellipsoids yields more elliptical and prolate shapes than fitting spheres.

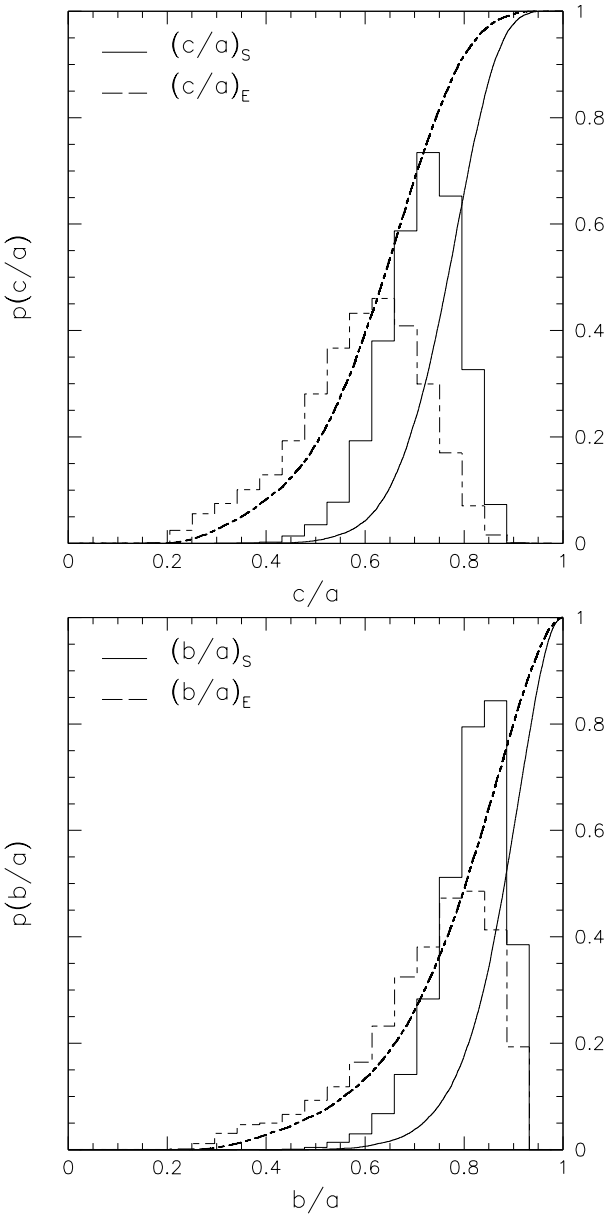


**Figure 4.** Cumulative and differential distribution of axial ratios $c/a$ and $b/a$ at the virial radius, from fitting ellipsoids (dashed) and spheres (solid). Ellipsoidal haloes have a smaller median value, with significantly more objects at small $b/a$ and/or $c/a$. This difference is more significant for $c/a$, meaning that haloes become more prolate when fit with ellipsoids.

given time, to check if (a) the shape depends on mass and (b) if, at fixed mass, the shape varies as a function of distance from halo center. We find that massive haloes are less round than lower mass haloes since this agrees with previous work (Jing & Suto 2002; Allgood et al. 2006), we do not show plots here. Our analysis also confirms the general opinion that, on average, there is also a systematic dependence of shape on radius: haloes are more elongated closer to the center, and more spherical in the outskirts (Allgood et al. 2006; Jing & Suto 2002; Warren et al. 1992). In addition, more massive haloes have a steeper gradient in axial ratios than lower mass haloes: this happens because the more massive haloes are less influenced by their environment.

We also measured the misalignment between the axis direction at a certain fraction of the radius and the axis at $0.5r_{vir}$. For this, we choose a subsample of the haloes, restricting our analysis to those for which the axes direction is determined more precisely. For this purpose we define the accuracy in the axis determination by

$$\theta_{err} = \frac{1}{2\sqrt{N}} \frac{\sqrt{r}}{1-r} \,\mathrm{rad} < 0.1\,\mathrm{rad} \qquad (10)$$

where $N$ is the number of particles used and $r$ is the relevant axial ratio: $b/a$ for the major axis, $a/b$ for the minor axis, and $\max[b/a;\, a/b]$ for the intermediate axis (Bailin & Steinmetz 2004, 2005). Notice that the alignment is slightly better for more massive haloes, represented by the black curve, but on average the internal alignment is very good, confirming previous results (Jing & Suto 2002; Bailin & Steinmetz 2005; Vera-Ciro et al. 2011; Schneider et al. 2012).

## 5 PROTOHALOES AND THE INITIAL FIELD

We have discussed the differences between spherical and ellipsoidal haloes, comparing the halo properties at the present time, when the haloes are collapsed and virialized. We now study these differences for proto-haloes in the initial conditions.

The protohalo regions are defined by tracing all halo particles, identified at $z = 0$, back to their unperturbed (Lagrangian) positions. For each protohalo we calculate the elements of the deformation tensor, defined at each position $\mathbf{q}$ as the second derivatives of the gravitational potential $\Phi$. This, in the the Zel'dovich approximation (Zel'dovich 1970) is equivalent to the evaluation of the first derivatives of the initial displacement:

$$\xi_{ij}(\mathbf{q}) = -\frac{\partial^2\Phi}{\partial x_i \partial x_j}(\mathbf{q}) = -\frac{\partial\Psi}{\partial x}. \qquad (11)$$

These were calculated from the initial displacement grid and differentiated with respect to the spatial coordinates.

Specifically, for each halo we flagged the grid points occupied by particles and calculated the deformation tensor as:

$$\xi_{ij} = \frac{1}{V_L}\int_{V_L} \xi_{ij}(\mathbf{q}) d^3x = \frac{1}{N_G}\sum_{k=1}^{N_G} \xi_{ij}(k) \qquad (12)$$

where $N_G$ is the sum of all the grid cells contained within the lagrangian volume of the halo: i.e., those actually occupied by halo particles and those left empty, but still located inside the halo (with at least four neighbor cells occupied by particles). These last must be considered since the total potential field acting on the halo is affected by their contribution. Thus, we used an algorithm to select the correct set of empty cells and added their contribution to the deformation tensor of the halo. This results in a small change to the original value, which refines the one obtained using the particle grid points only. Since the shape of the protohalo regions is not symmetric nor regular, we could not choose a characteristic radius and use it to smooth the distribution in Fourier space (and calculate the value od the deformation tensor from it), since we need to maintain spatial resolution at each point.

While doing this, we also studied the profiles of haloes in the initial conditions. Since the particles belonging to each halo are selected at the present time, they do not necessarily form a single simply connected *lump* in the initial conditions. We found that haloes are indeed more fragmented in the initial conditions, but in most cases the mass of the main lump is more than 90% of the total mass of the halo. Thus, to calculate the initial properties, we decided to use the particles contained in the main lump, and to exclude from our sample those haloes for which less than 90% of the mass is in the main lump. (In some rare cases, this fraction can be as small as 50% of the mass: these haloes probably formed through a recent merging process or have undergone some transformations in time, so they do not correspond to a sufficiently compact region in the initial conditions. They are only 8% of the total sample: removing them does not affect the mean behavior, but it does reduce the scatter around this mean.) Summing up, $N_G$ is the sum of all the cells (full and empty) contained in the main lump of the each halo.

| $\nu$ | mass | n |
|---|---|---|
| 0.53 | $M_\star/16$ | 6607 |
| 0.67 | $M_\star/4$ | 3890 |
| 0.84 | $M_\star$ | 1061 |
| 1.06 | $2 - 4M_\star$ | 348 |
| 1.33 | $8 - 16M_\star$ | 109 |

**Table 1.** Correspondence between mass bins and $\nu$; $M_*$ is $8.956 \times 10^{12} M_\odot h^{-1}$. The third column shows the number of haloes in each bin.

### 5.1 Non-positivity of the initial eigenvalues

Figure 5 shows the distribution of the $\lambda_i$ as a function of halo mass, which we express in scaled units $\nu = \delta_{sc}/\sigma(M)$, where $\sigma^2(M)$ represents the variance in the initial density fluctuation field when smoothed on scale $R = (3M/4\pi\bar{\rho})^{1/3}$ (the $\lambda_i$s are rescaled to $z = 0$ to allow an easier comparison with the distribution of $\delta_i$ shown in Figure 6). In principle, this expression assumes a spherically symmetric filter. Although (Lam & Sheth 2008) provide the relevant expression for non-spherical filters, and note that it only makes a small difference, our main purpose here is to rescale the mass variable, so using the spherical expression is appropriate. In these units, $\nu = 1$ corresponds to a mass $M_*$ is $8.956 \times 10^{12} M_\odot h^{-1}$. Later on, we will study halo properties for broader bins in mass; Table 1 shows the correspondence between these mass bins and $\nu$.

Figure 5 shows that while the first and the second eigenvalues are mostly positive, the third one is negative for the majority of the haloes, especially at lower masses. This indicates that, on average, protohaloes in the initial conditions are not contracting with the same strength along all their axes, and that, in the direction of $\lambda_3$ the potential may act slowing down the contraction. (We note in passing that $\lambda_3 < 0$ directly contradicts the fundamental assumption of Lee & Shandarin (1998)'s model of halo abundances, meaning their model is untenable.) More precisely, only 30% show $\lambda_{1,2,3} \geqslant 0$, while 70% have $\lambda_3 \leqslant 0$ and $\lambda_{1,2} \geqslant 0$. A small fraction ($< 1\%$) of haloes behave very differently from these two categories.

So far we have checked the differences between ellipsoidal and spherical identification as far as mass and final shape are concerned. It is natural to ask how the corresponding initial deformation tensors differ. We found that, as for the mass, the two identification schemes yield very similar results: although there are haloes (especially at low mass) with significant differences, even larger than 40%, the median of the distributions remains around zero. The variance is larger in the case of $\lambda_3$, and, of course for lower masses. This shows that the spherical overdensity criterion traces

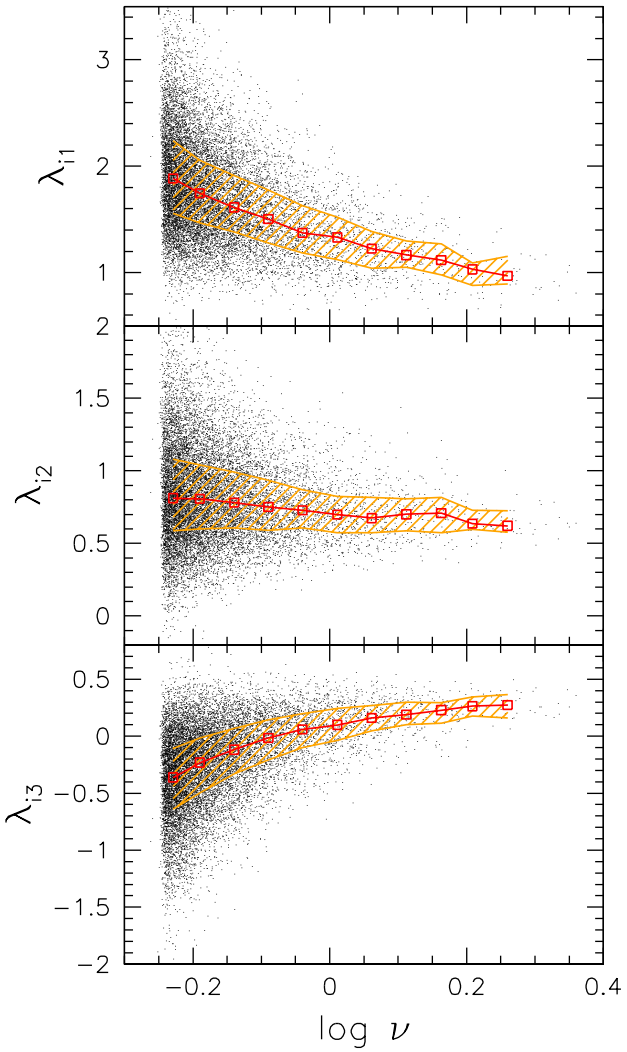


**Figure 5.** The eigenvalues of the deformation tensor for the ellipsoidal proto-haloes, as a function of mass (which has been scaled to $\nu$). The median of each distribution is shown in red, while the orange shaded region lies between the first and the third quartiles. Note that, while the first two eigenvalues are positive, the third one is almost always negative, especially at low mass, indicating that haloes are not contracting with the same strength along all the three directions and that the potential along the third axis may slow down the contraction in that direction.

the potential (and so the mass) quite well and that the best fitting ellipsoid is useful mainly for the description of the geometrical shape of the haloes and its evolution. The greater discrepancy for the values of $\lambda_3$, which is the one showing an unexpected behavior, suggests that our new procedure provides a more realistic description of the halo structure.

### 5.2 Protohalo overdensities: The trace of the initial deformation tensor

In the EC model, the fundamental quantities which influence the evolution are not the eigenvalues of the deformation tensor themselves, but the combinations $\delta, e, p$. The most important of these is the overdensity $\delta$, which is the trace of the deformation tensor.

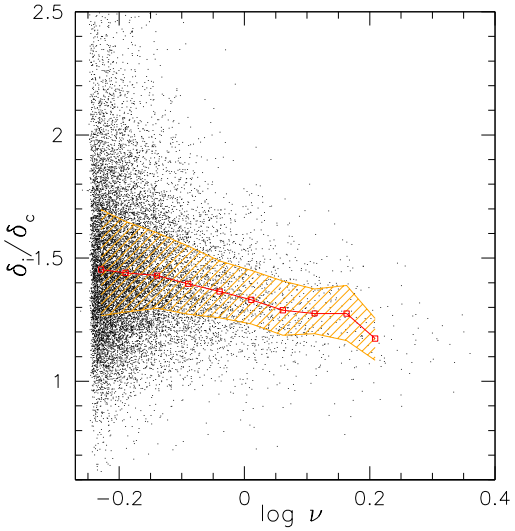


**Figure 6.** Distribution of the initial overdensity as a function of halo mass (here scaled to $\nu$). The overdensity is expressed in units of the critical value in the SC model, for ease of comparison with the EC prediction that it should always be greater than $\delta_{sc}$, and increasingly so at small masses.

Figure 6 shows the distribution of $\delta$ as a function of halo mass, here scaled to $\nu = \delta_{sc}/\sigma(m)$. For ease of comparison with equation (3), the overdensity within the initial protohalo has been rescaled to the present time using the linear growth factor $D_+(z=0)/D_+(z=49) = 38.993$. It is clear that the initial overdensity is a decreasing function of mass, in qualitative agreement with previous work (Sheth et al. 2001; Robertson et al. 2009), and with the prediction which comes from combining the *EC* model with the statistics of Gaussian random fields (Sheth et al. 2001). The required overdensity for collapse is higher for low mass haloes which must be able to hold themselves together against tidal effects. Although the overdensity values can be substantially higher than the critical value associated with the SC model, especially at small masses, they are almost never smaller. This represents a nontrivial success of the EC model.

Qualitative success does not guarantee quantitative agreement. In the EC model, the initial density of protohalo regions depends on the shape parametes $e$ and $p$ (equation 3). A simple estimate of the mass dependence comes from replacing $e\delta$ and $p\delta$ in equation (3) with a naive estimate of their mean values. If averaged over all possible positions in a Gaussian field, this gives $\sigma/\sqrt{5}$ and zero as characteristic values of $e\delta$ and $p\delta$, making $\delta/\delta_{sc} = 1 + \beta\,\nu^{-2\gamma} = 1 + 0.25\,\sigma^{1.2}$. The median values shown in Figure 6 are smaller than this most naive prediction.

Most of the mass dependence in Figure 6 is removed by rescaling to $\Delta_h \equiv (\delta/\delta_{sc} - 1)/\sigma$. Figure 7 shows that, in these scaled units, the mean and rms values are approximately 0.2 and 0.12. These values are smaller than those reported by Robertson et al. (2009) ($0.48/\delta_c = 0.28$ and $0.3/\delta_c = 0.18$). Some of this is due to the fact that we use the actual particle distribution in the initial conditions to determine $(\delta, e, p)$, rather than assuming the initial shape was spherical. In addition, we use EO rather than SO de-

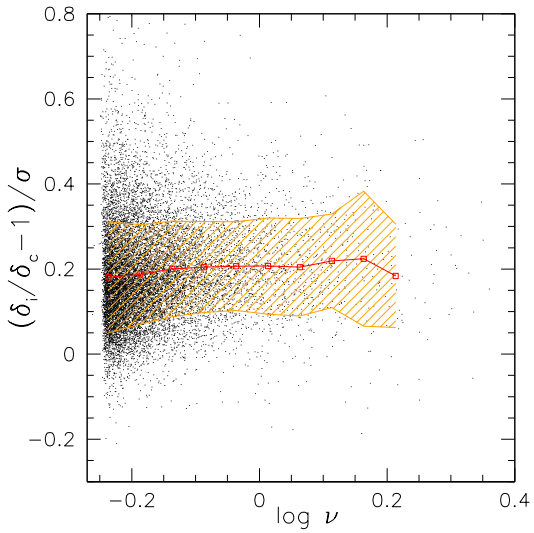


**Figure 7.** Same as previous figure, except that now the initial overdensity has been scaled to $\Delta_h$, in terms of which most of the mass dependence has been removed.

rived quantities. We believe these differences matter, since the shape of the distribution is expected to encode information about the quantities in the initial conditions which determine halo formation.

### 5.3 Ellipticity and prolateness of the deformation tensor

In the EC model, the fundamental quantities which influence the evolution are not the $\lambda_j$ themselves, but the combinations $\delta, e, p$. Since we have already discussed $\delta$, we now turn to a study of $e$ and $p$ in our protohaloes. Recall that, if the shape is caused entirely by the deformation tensor, then a prolate mass configuration corresponds to $p < 0$ and an oblate one to $p > 0$. (This classification differs from the one given by the geometrical mass distribution, in which a physically prolate/oblate halo has $p > 0/p < 0$.)

The distributions of ellipticity and prolateness are shown in the two panels of Figure 8 as a function of halo mass (always represented by $\nu$). Recall that the combination of the EC model with Gaussian field statistics means that lower mass haloes should, on average, have larger values of $e$ with a larger rms around this mean, while the most naive averaging procedure suggests that $e\delta/\sigma$ should have mean $\approx 1/\sqrt{5} = 0.447$ and rms 0.14 independent of mass. The lack of mass dependence in the mean and rms values is in good agreement with our measurements, although their actual values, 0.4 and 0.13, are slightly smaller than predicted. Similarly, $p\delta/\sigma$ has mean zero as predicted, but the measured rms of 0.15 is smaller than the predicted value of 0.22.

Inserting these values to obtain the EC prediction for the typical overdensity of protohaloes yields $\delta/\delta_{sc} = 1 + \beta\,(4/5)^\gamma \nu^{-2\gamma} = 1 + 0.22\,\sigma^{1.2}$. Comparison with the bottom panel of Figure 8 shows that this is about 10% higher that what we see. Our measurements indicate that $\delta/\delta_{sc} - 1 \approx 0.2\sigma$, with an rms scatter around this mean of $0.12\sigma$ (also see Figure 7).

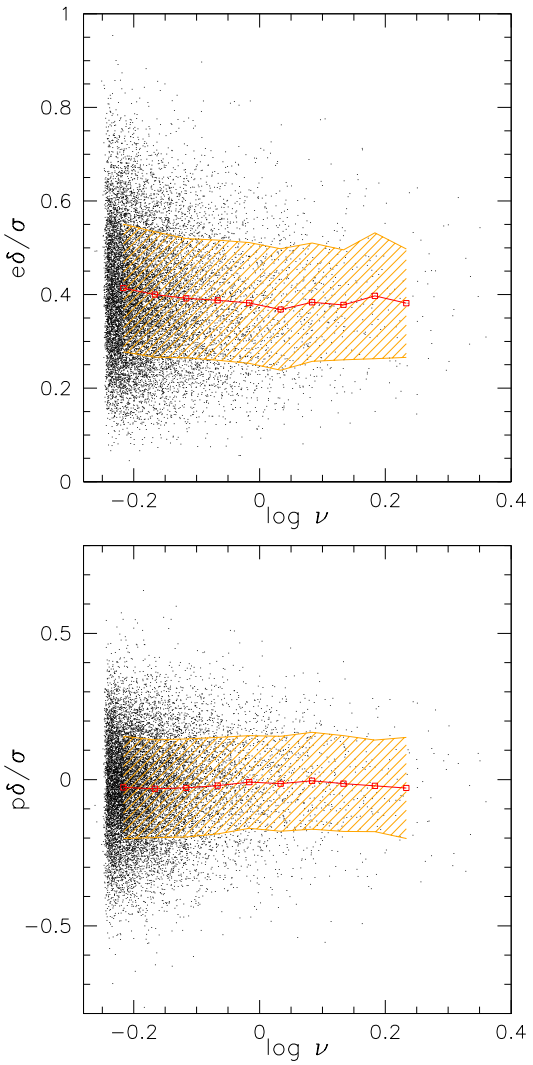


**Figure 8.** Distribution of the initial ellipticity and prolateness of the haloes as a halo mass (here scaled to $\nu$). $e$ and $p$ have been scaled by $\delta/\sigma$ for more direct comparison with the EC prediction that $e\delta/\sigma$ and $p\delta/\sigma$ should be independent of protohalo mass.

Before moving on, note that $e\delta \equiv (\lambda_1 - \lambda_3)/2$, so, on average, $\lambda_1 - \lambda_3 \sim 0.8\sigma$. In addition, $p = 0$ implies $\lambda_1 + \lambda_3 = 2\delta/3$ or $\lambda_1 - \lambda_2 = \lambda_2 - \lambda_3$. While this latter is interesting itself, it is also worth noting that the mean values we see imply mean values of $\lambda_1 = \delta/3 + 0.4\sigma$, $\lambda_2 = \delta/3$ and $\lambda_3 = \delta/3 - 0.4\sigma$. This shows that the mean value of $\lambda_3$ will be less than zero once $\sigma$ exceeds $5\delta/6$. Inserting the mean trend $(\delta/\delta_c - 1) \sim 0.2\sigma$ implies $\sigma \geqslant (5\delta_c/6)(1 + 0.2\sigma)$ or $\sigma \geqslant (5\delta_c/6)/(1 - \delta_c/6)$. So, a significant fraction of haloes with $\nu \equiv \delta_c/\sigma \leqslant (6 - \delta_c)/5 \sim 13/15$, will tend to have $\lambda_3 < 0$ (as shown in Figure 5).

Finally, Figure 9 shows the cumulative distributions of the three initial parameters, as a function of halo mass: the haloes were divided into five mass bins, described in Table 1. This confirms that, on average, both the initial overdensity $\delta$ and initial ellipticity $e$ are larger at small mass, while the initial prolateness $p$ is distributed around a mean value of zero.

We believe we have demonstrated that the combination

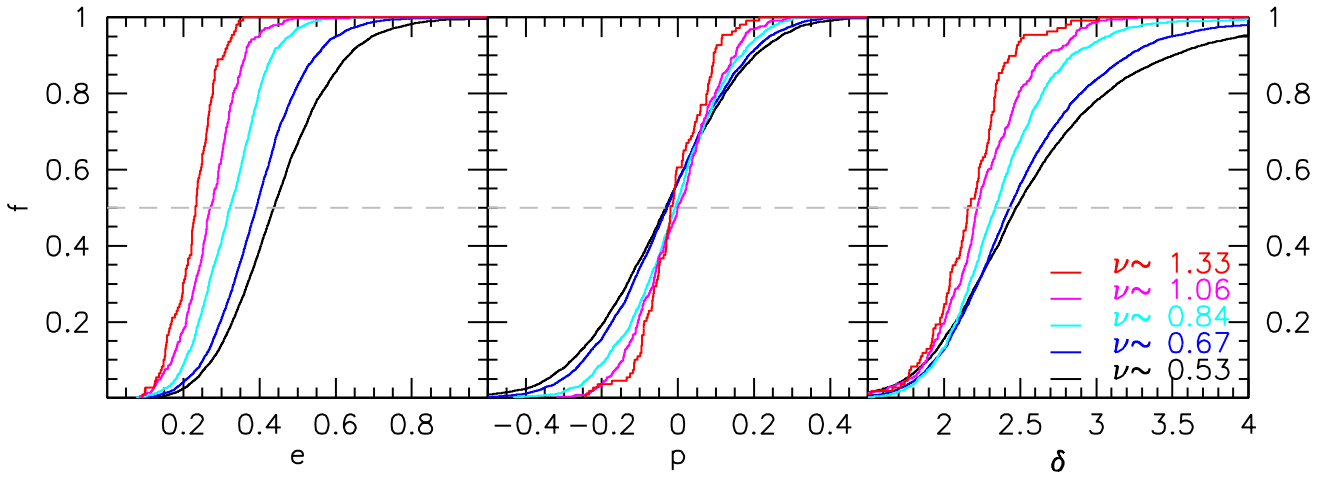


**Figure 9.** Cumulative distribution of initial ellipticity, prolateness and overdensity, for five different mass bins indicated by the colors; the bins have the same width in $\log(\nu)$. They clearly show that ellipticity is a decreasing function of mass, as is the overdensity. In contrast, prolateness is almost the same, on average, for all mass bins. The gray dashed line is drawn to help identify the median values in the cumulative distributions.

of the EC model with the statistics of the Gaussian potential field works reasonably well. Because the potentials of the most massive proto-haloes are indeed more spherical, whereas the shapes of the most massive virialized haloes are less spherical, we conclude that we have a puzzle. Either the EC model is incorrect in its description of the evolution, or the proto-haloes are non-spherical even initially, and this influences the final shapes.

## 6 HALO SHAPES

The simplest *EC* model assumes that haloes evolve and collapse through a series of triaxial configurations; the directions of the three axes of the ellipsoid do not change, and they are determined by the initial deformation tensor. Therefore, the mass tensor is perfectly correlated with the initial (Lagrangian space) tidal tensor. In what follows, we first show that the shapes are not spherical initially. This raises the question of whether or not the EC assumption that the directions of the principal axes of the mass and deformation are aligned is justified. We address this in the second half of this section.

Although we speak of the principle axes of the two tensors, it is clear that their physical meaning is different: the eigenvalues and eigenvectors of the mass tensor give an estimate of the actual particle distribution at a given time, thus describing the physical *shape* of the halo; whereas those of the deformation tensor, calculated at the initial time, describe the characteristics of the gravitational potential field within and around protohaloes and so are used to predict how the protohalo shape will change in time.

### 6.1 Triaxiality of initial shapes

Recall that, in the simplest EC model, the initial mass distribution was spherical, so the mass tensor at any later time is determined completely by the initial tidal tensor defined by its constituent particles. Figure 10 shows that the protohaloes are not spherical: the axis ratios as determined from the square-roots of the initial mass tensor only approach unity for the most massive haloes.

### 6.2 Initial alignment of the mass and deformation tensors

To quantify the correlation between the mass and deformation tensors, we study the the distribution of $\mu_{ij} = |\cos(\widehat{\lambda_i l_j})|$, the cosine of the angle between axis $i$ and $j$ of the initial deformation and mass tensors. Recall that the deformation tensor eigenvalues are ordered, as in the previous Sections, as $\lambda_1 \geqslant \lambda_2 \geqslant \lambda_3$; we use $l_i$ ($l_1 \geqslant l_2 \geqslant l_3$) for the three axes calculated from the mass tensor (here we prefer to call them $l_i$ instead of $a, b, c$, for uniformity of notation with the $\lambda_i$s). The directions are said to be correlated if they are well-aligned ($\mu_{ij} \simeq 1$), while they are *anticorrelated* in the opposite case ($\mu_{ij} \simeq 0$): the maximum misalignment happens when the two vectors (representing the semi-axes of the ellipsoid) are perpendicular to each other, while they are considered aligned when $\cos(\widehat{\lambda_i l_j}) \simeq 1, -1$, since a misalignment of more than 90 degrees corresponds in fact to an alignment on the other side.

Previous work (measurements in simulations) has shown that while this correlation is indeed very good, the two tensors are not perfectly correlated (Porciani et al. 2002). Figure 11 confirms this. For our protohaloes, the longest axis of the mass tensor $l_1$ is very well-aligned with $\lambda_1$ of the deformation tensor, which corresponds to the direc-

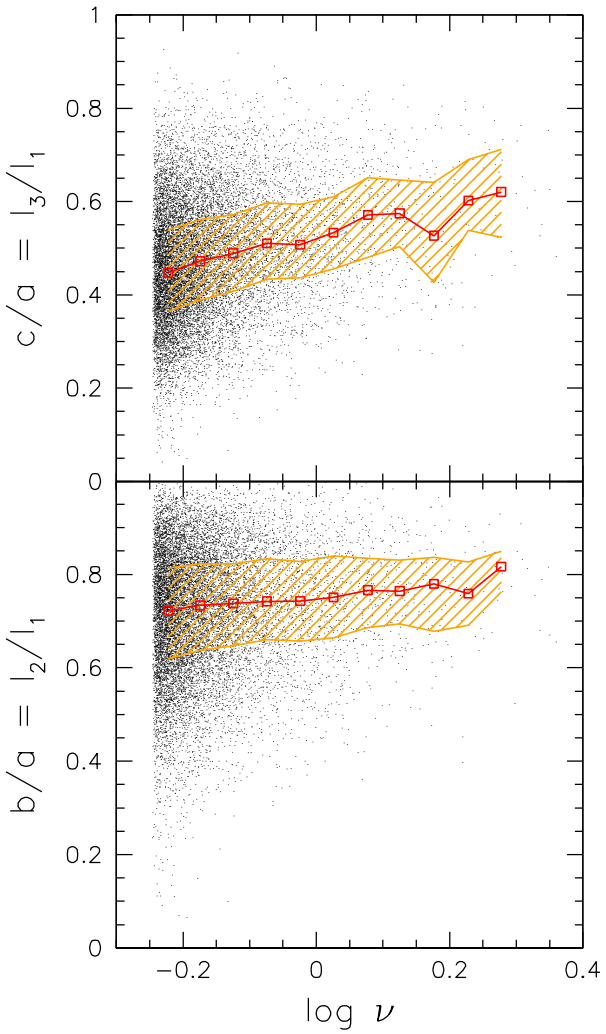


**Figure 10.** Axis ratios calculated from the square root of the mass tensor eigenvalues of the protohaloes at the initial time.

tion of maximum compression; similarly the shortest mass tensor axis $l_3$ is aligned with the direction of minimum compression $\lambda_3$. To quantify this, the median values of the distributions in Figure 11 are:

$$p[\cos(\theta_{ij})] = \begin{pmatrix} 0.898 & 0.396 & 0.081 \\ 0.406 & 0.853 & 0.109 \\ 0.070 & 0.120 & 0.985 \end{pmatrix}. \qquad (13)$$

Thus, it is no longer obvious that the halo will turnaround first along the direction of its initial major mass axis, then along the second and finally along the third mass axis. Rather, the differences in the turnaround (or collapse) times of the three axes may be smaller than they were for the case of collapse from a sphere.

### 6.3 Alignment of the final mass tensor with the initial deformation tensors

Therefore, it is also interesting to study the alignment between the initial and final axes to check how the evolution affects the axis orientation. At the initial time, both the

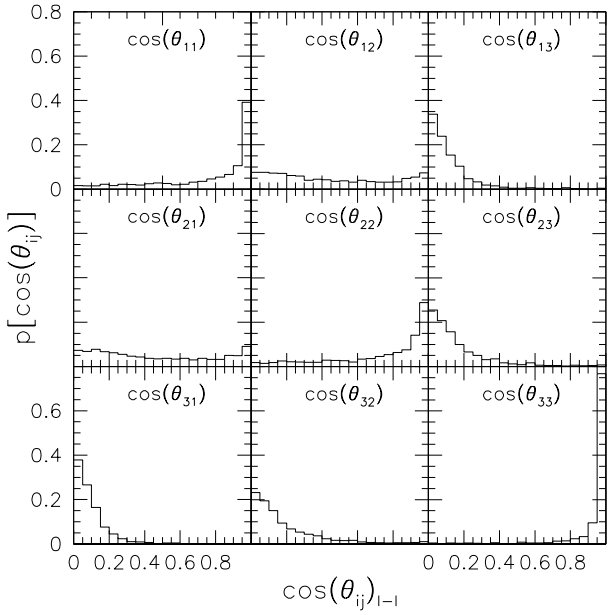


**Figure 11.** Alignment between the principal axes of the initial mass tensor and the initial deformation tensor.

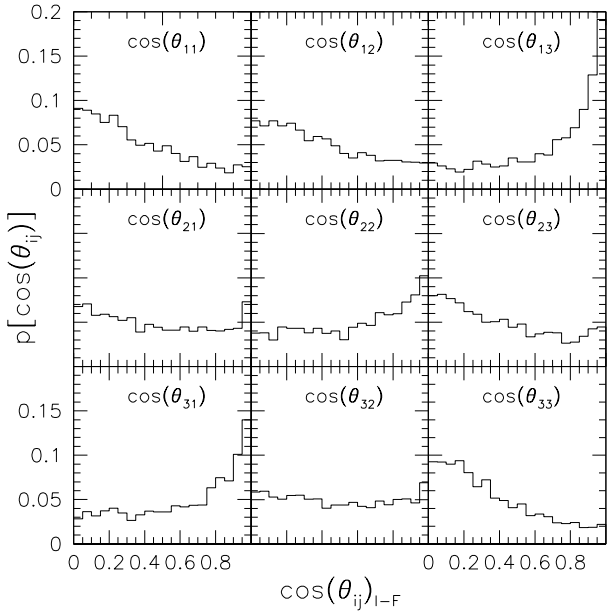


**Figure 12.** Alignment between the principal axes of the initial deformation tensor and the final mass tensor.

mass and the deformation tensor can be used to approximate protohaloes, while the final orientation and dimension of the haloes can be described only by the mass distribution (since the Zel'dovich (1970) approximation used to calculate the $\lambda_i$ can be applied only at the initial time). Hence, Figure 12 compares the alignments between the principal axes of the final mass tensor with that of the initial deformation tensor.

For this particular analysis we only chose haloes with more than 1000 particles - so as to ensure accurate determination of the mass eigenvectors - and haloes with smooth evolution and mass accretion history. This last condition

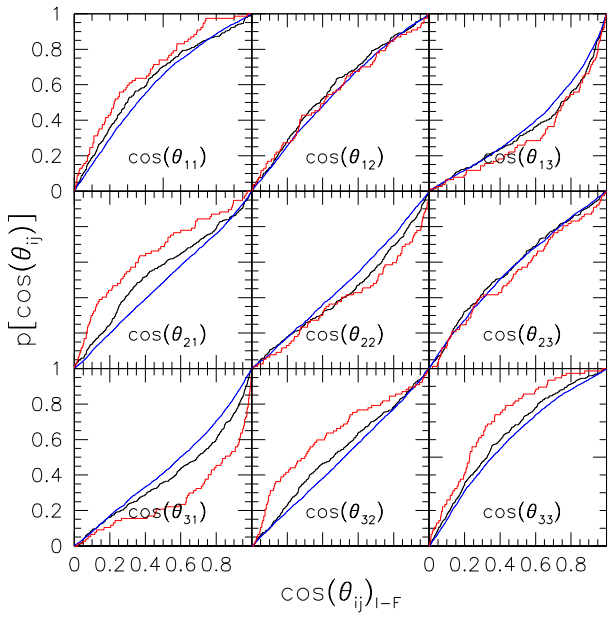


**Figure 13.** Same distributions as in Figure 12, but in cumulative rather than differential form; haloes are now split according to their mass: $M_\star/16$ in blue, $M_\star$ in black and $8-16M_{star}$ in red. The alignments or misalignments are enhanced at higher masses.

arises because we have found that a significant fraction of haloes presents an irregular evolution history, probably due to the occourence of important merging events, which of course influence the final orientation of the halo. We identified these using an objective automated algorithm, which searches for irregularities in the evolution of the amplitudes of the axes of the best fitting ellipsoid. We exclude them from the sample for this specific case, because their final properties could be influenced by the merging history more than by the initial distribution, unlike regular haloes. Thus, they constitute a different population which should be studied separately, as we intend to do in a future work.

Returning to Figure 12, it is clear that at the final time the axes of the two tensors are not so well-aligned as in the initial conditions: the top-right box, for $\cos(\theta_{13}) = \cos(\widehat{\lambda_{I1} l_{F3}})$, shows that the final shortest axis of the mass tensor seems to be aligned with the direction of initial maximum compression $\lambda_1$. The bottom right panel shows that it is almost anticorrelated with the direction of initial minimum compression. This sort of inversion occurs also in the case of the first axes: the bottom-left box shows that the final longest mass axis $l_{F1}$ is better aligned with $\lambda_3$ than with $\lambda_1$ (top-left box).

The tendency shown in Figure 11 is thus completely reversed. Now, the median values of the (cosines of the) alignment angles are:

$$p[\cos(\theta_{ij})] = \begin{pmatrix} 0.310 & 0.360 & 0.779 \\ 0.463 & 0.613 & 0.365 \\ 0.677 & 0.497 & 0.300 \end{pmatrix} \qquad (14)$$

confirming that whereas before the 11 and 33 correlations were strongest, now it is the 13 and 31 correlations which are strongest.

### 6.4 Mass dependence

Figure 13 shows how this behaviour depends on halo mass, plotting the same distributions of Figure 12 (but here cumulative and not differential) for haloes of three mass bins: black, blue and red curves show results for mass bins centered on $M_\star$, $M_\star/16$ and $8-16M_\star$. Clearly, the evolution pattern that we have suggested is strongest for the most massive haloes.

We also checked the alignment between the initial and final axes of the mass tensor, but we do not present the result here since the correlations are weaker and only the behavior of the shortest axis is well defined: this seems to indicate that the potential field is a better tracer of the initial shape, since it shows what will be the evolution tendency more than the actual initial position of particles.

### 6.5 Evolution

To study more closely if and when the axes invert, Figure 14 shows the evolution of the misalignment between the major axis of initial deformation tensor $\lambda_{I1}$ and the shortest axis of the mass tensor $l_3$ (i.e., the strongest alignment shown in equation 14) calculated at each time step of the simulation. The points show the median value of the cosine of the angle between the principal axes of the two tensors at each time and he dashed lines the first and third quartiles of the distribution. At high redshift the two axes are almost perpendicular to each other, but by $z = 0$ they are almost perfectly aligned. I.e., the halo collapses in the direction of maximum compression and, by the end, the shortest axis of the halo lies in this direction (which is almost perpendicular to the direction of the initial shortest axis). There is, in fact, an intermediate period of rapid misalignment, followed by a stable period at late times.

We believe that this inversion in direction is rather generic to the collapse process, but there are a number of ways in which this can happen. If the mass and deformation tensors are perfectly aligned, then this is just a consequence of the compression due to the tidal field. I.e., early-on, the protohalo contracts most rapidly along the direction of $\lambda_1$, while contracting more slowly along the direction of $\lambda_3$. Eventually, the protohalo collapses first along the direction of $\lambda_1$, then along $\lambda_2$ and finally along $\lambda_3$; the resulting mass distribution ends up being more compressed along the direction of maximum initial compression, $\lambda_1$, and more elongated in the direction of initial minimum compression $\lambda_3$. As a result, the longest axis of the mass tensor of the final object, which is perpendicular to the shortest axis, ends up being perpendicular to its initial direction, even though there is no rotation. In this case, there should be a time during the evolution when the axis lengths are equal.

If the mass and deformation tensors are not well-aligned initially, then the object may rotate. For example, if the second axes are well-aligned but the first and third are not, then the object may rotate about the second axis. This rotation will be most effective if the sum of the first and third deformation vectors is perpendicular to the sum of the first and third mass vectors. I.e., rotation will be most efficient if $\lambda_1$ and $\lambda_3$ have opposite signs. Once the axes are aligned, the rotation stops. In this case, the exchange of direction of the axes need not be accompanied by an exchange of lengths.

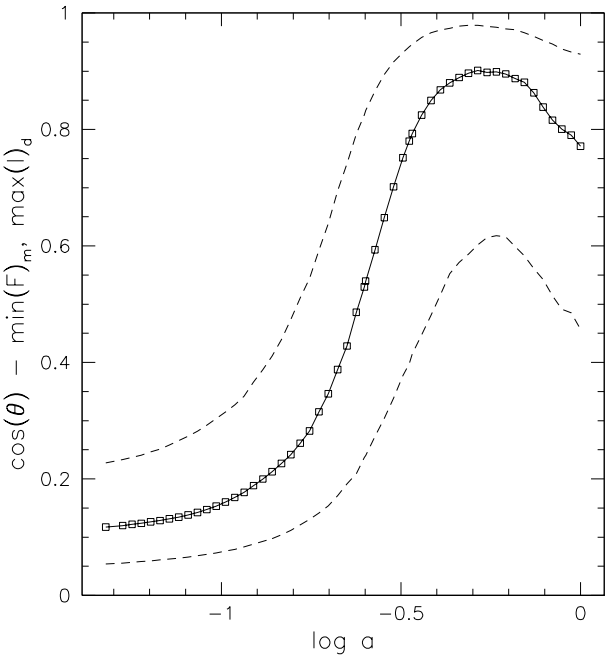


**Figure 14.** Misalignment between the longest axis of initial deformation tensor and the the shortest axis of the mass tensor of the haloes at as a funcion of time, represented by log(a): the points represent the median values at each time and the dashed lines the first and third quartiles of the distribution.

Note that although we showed that $\mu_{11} \sim 1$, suggesting that the initial misaligments are small, $\mu_{11} = 0.9$ still allows misalignments as large as 20°. Since the rotation depend on the cross- rather than dot-product of the two vectors, rotation might be more common than one might have concluded on the basis of the statement that $\mu_{11} \sim 1$.

Finally, there could be an intermediate case: it may be that the halo does not actually rotate, in the sense of having an overall angular momentum: rather, as the particle distribution is squeezed by different amounts in different directions, the relative lengths of the mass axes change, the particle distribution deforms (maybe not exactly along the directions of the $\lambda_i$s due to the initial misalignment between the two tensors) and so the direction in which the longest axis points can evolve.

In summary: the major axis of a protohalo is initially aligned with the direction of maximal compression (Porciani et al. 2002, in agreement with). For a few haloes, the compression is sufficiently large that this longest axis ends up being the first one to turnaround and collapse, and so it becomes the shortest axis. Whether or not the axis lengths invert, for most haloes, the axis directions do: the shortest axis of the final object ends up being well-aligned with the initial direction of maximal compression.

## 7 SUMMARY AND CONCLUSIONS

To study the shape and evolution properties of dark matter haloes, we analysed a sample of simulated haloes extracted from the GIF2 simulation (Gao et al. 2004). First, we showed how the way in which haloes are identified affects conclusions about their shapes, and of the proto-halo patches from which they formed.

In Section 3 we presented an algorithm which identified dark matter haloes as triaxial ellipsoids enclosing the virial overdensity assumed by theory. In Section 4 we showed that:

- Compared to the usual spherical overdensity method, haloes identified using our *Ellipsoidal Overdensity* method are more massive, because a triaxial shape is able to trace the density distribution better than a sphere. However, this difference is typically less than 10%.
- The change to the final halo shape is more significant, with differences in the axial ratios as large as 40%, leading to more elliptical (and in particular more prolate) shapes: our *Ellipsoidal Overdensity* criterion refines halo shapes, making them more varied and realistic.

In Section 5 we studied the corresponding protohaloes in the initial conditions. We checked how the EO algorithm affects protohalo properties, showing that the eigenvalues of the deformation tensor have a slightly broader distribution, but otherwise exhibit the same trends as for protohaloes of SO haloes. This suggests that the initial potential field is less affected by the selection algorithm.

In the EC model, the properties of the initial field are expressed not in terms of the three eigenvalue of the deformation tensor $\lambda_i$ but using the trace, and the shape parameters $e$ and $p$. We plotted their distributions, finding that:

- for most protohaloes the eigenvalues of the deformation tensor do not have the same sign; the fraction of protohaloes for which this is true increases at low masses;
- at fixed mass, protohaloes have a range of initial overdensities; these are almost always larger than the critical overdensity associated with spherical collapse; the mean overdensity increases as mass decreases, scaling approximately as $\delta_c(1+0.2\sigma)$, and the rms distribution around this mean is $0.2\sigma$ (it is broader for lower mass haloes);
- the median ellipticity $e$ of the deformation tensor decreases as mass increases: the distribution of $e\delta/\sigma$ is approximately independent of halo mass, having mean $\sim 0.4$ and rms 0.14;
- the median prolateness of $p\delta/\sigma \simeq 0$ with rms 0.15;
- the mass tensors are increasingly non-spherical as protohalo mass decreases.

The middle three findings are in good qualitative agreement with the triaxial collapse model in which low mass haloes need a higher initial overdensity so as to collapse by the present time, because they tend to be less spherical.

The final part of this work aimed at understanding how the initial potential field interacts with haloes and influences their evolution, since the initial properties are the dominant ingredient in the *EC* model. Thus, we studied the cross-talk between the mass tensor and the deformation tensor: the first gives an estimate of the particle distribution of haloes and so of their actual shape and orientation, while the second (calculated only at the initial time) describes the potential field. We showed that:

- At the initial time, the principal axes of the two tensors are very well-aligned; the longest axis of the mass tensor ($l_1$) is aligned with the direction of maximum compression $\lambda_1$, $l_2$ is aligned with $\lambda_2$, and $l_3$ with $\lambda_3$. However, although cos

of the misalignment angle is $\sim 1$, the angle itself can still be of order tens of degrees.

- At the final time ($z = 0$) the alignment between the axes is reversed, as a consequence of the collapse process and the associated deformation of the particle distribution.
- The change in directions of the first and third axes are sometimes dominated by the different compression factors, and others by what appears to be rotation, although it is still unclear if the apparent rotation is actually an asymmetrical deformation of the particle distribution.

Whereas the initial alignment is common in models where haloes form from peaks in the initial density field, the order of the alignments is opposite to that for peaks, which predict alignments which are more like those we see for final haloes.

These late time alignments, which suggest that the direction of maximal compression remains approximately constant as the halo collapses and its shape changes, are consistent with recent measurements of anisotropies in the halo-mass clustering signal, which indicate that the long axes of virialized haloes are aligned with the large scale structures in which they are embedded (Faltenbacher et al. 2012). Moreover, a model which explicitly assumes this (lack of evolution of the deformation tensor) to be true appears to provide a good description of these measurements (Pápai & Sheth 2012). We plan to study further whether it is deformation or rotation which is the cause of the change in alignments we see.

## ACKNOWLEDGMENTS

GD was funded by PhD grants at the University of Padova. RKS was supported in part by NSF-0908241 and NASA NNX11A125G.

## REFERENCES

Allgood B., Flores R. A., Primack J. R., Kravtsov A. V., Wechsler R. H., Faltenbacher A., Bullock J. S., 2006, MNRAS, 367, 1781
Bailin J., Steinmetz M., 2004, ApJ, 616, 27
Bailin J., Steinmetz M., 2005, ApJ, 627, 647
Bett P., Eke V., Frenk C. S., Jenkins A., Helly J., Navarro J., 2007, MNRAS, 376, 215
Bond J. R., Myers S. T., 1996, ApJS, 103, 1
Desjacques V., 2008, MNRAS, 388, 638
Eke V. R., Cole S., Frenk C. S., 1996, MNRAS, 282, 263
Faltenbacher A., Li C., Wang J., 2012, ApJ, 751, L2
Gao L., White S. D. M., Jenkins A., Stoehr F., Springel V., 2004, MNRAS, 355, 819
Giocoli C., Moreno J., Sheth R. K., Tormen G., 2007, MNRAS, 376, 977
Giocoli C., Tormen G., van den Bosch F. C., 2008, MNRAS, 386, 2135
Gunn J. E., 1977, ApJ, 218, 592
Jing Y. P., Suto Y., 2002, ApJ, 574, 538
Kauffmann G., White S. D. M., 1993, MNRAS, 261, 921
Lacey C., Cole S., 1993, MNRAS, 262, 627
Lacey C., Cole S., 1994, MNRAS, 271, 676
Lam T. Y., Sheth R. K., 2008, MNRAS, 389, 1249
Lee J., Shandarin S. F., 1998, ApJ, 500, 14
Pápai P., Sheth R. K., 2012, ArXiv e-prints
Porciani C., Dekel A., Hoffman Y., 2002, MNRAS, 332, 339
Robertson B. E., Kravtsov A. V., Tinker J., Zentner A. R., 2009, ApJ, 696, 636
Rossi G., Sheth R. K., Tormen G., 2011, MNRAS, 416, 248
Schneider M. D., Frenk C. S., Cole S., 2012, JCAP, 5, 30
Seljak U., Zaldarriaga M., 1996, ApJ, 469, 437
Shen J., Abel T., Mo H. J., Sheth R. K., 2006, ApJ, 645, 783
Sheth R. K., Mo H. J., Tormen G., 2001, MNRAS, 323, 1
Sheth R. K., Tormen G., 2002, MNRAS, 329, 61
Springel V., White S. D. M., Tormen G., Kauffmann G., 2001b, MNRAS, 328, 726
Tormen G., Moscardini L., Yoshida N., 2004, MNRAS, 350, 1397
Vera-Ciro C. A., Sales L. V., Helmi A., Frenk C. S., Navarro J. F., Springel V., Vogelsberger M., White S. D. M., 2011, MNRAS, 416, 1377
Warren M. S., Quinn P. J., Salmon J. K., Zurek W. H., 1992, ApJ, 399, 405
White S. D. M., 1996, in Schaeffer R., Silk J., Spiro M., Zinn-Justin J., eds, Cosmology and Large Scale Structure Formation and Evolution of Galaxies. p. 349
White S. D. M., Silk J., 1979, ApJ, 231, 1
Zel'dovich Y. B., 1970, A&A, 5, 84

## APPENDIX A: EVOLUTION OF THE PARTICLE DISTRIBUTION

The main text described the mean behavior of the halo population. This mean behaviour is indeed representative of individual haloes. To illustrate this, we show how the shape and orientation of the particle distribution in a few representative haloes evolves.

Since the deformation and mass tensors are not aligned in general, the objects may rotate as well as deform, so we must make some choices about how we describe the evolution. We have chosen to show two dimensional projections of the particle distributions with respect to a fixed coordinate system. In addition, we show how the (square-roots of the) eigenvalues of the mass tensor evolve. These represent the lengths of the principal axes of the object; if two of these cross, then this signals that the compression due to the deformation tensor has managed to change the relative axis lengths. The main text argued that this is generic in the Zeldovich approximation with perfect alignment. This information about how the size of the object changes gives no insight into the spatial orientation of the object. To see if the principal axes of the mass tensor change direction – from the combined effects of compression and rotation – we also show how the angle between the mass tensor axis $l_i$ and the initial deformation tensor axis $\lambda_i$ evolves.

Figures A1 and A2 show the evolution of haloes of mass $M_*$and $16M_*$ respectively. Despite the order of magnitude difference in mass, both objects evolve rather similarly. In both cases, the initial particle distribution is rather non-spherical, after which gravitational collapse occurs along the preferred directions as discussed in the main text, creating a pancake; the directions of the three principal axes of the

best-fitting ellipsoid change with time; there is an *axis inversion* feature, such that the longest and shortest axes exchange directions. Notice that the evolution is not identical, even though the values of $\delta \sim 2$, $e \sim 0.2$ and $p \sim 0$ are approximately the same. This shows that the initial deformation tensor does not uniquely determine the evolution – the initial shape also matters, as does the degree of initial misalignment. For these haloes, $b/a$ and $c/a$ were $(0.94, 0.59)$ and $(0.91, 0.72)$, respectively, and although the initial alignments are all within $10^\circ$ for the first object, they are much worse for the second.

In more detail, the top panels show the projected particle distribution at nine time steps between $z = 49$ and $z = 0$. Red, magenta and yellow show the longest, intermediate and shortest axes of the mass tensor. Projecting from three to two dimensions means that the relative lengths are not always obvious in such a plot, so the bottom left panels show how the lengths of the three mass axes evolve. Red, blue and black curves show the evolution of the longest, intermediate and shortest axes, in units of

$$r_{\mathrm{L}i} \equiv (l_{1i} l_{2i} l_{3i})^{1/3}. \tag{A1}$$

In some cases (but not these), the axis which was initially the longest may become the second longest; this sort of length-inversion occurs in only a few of our haloes (which were excluded from the analysis regarding the axes alignments, to have a more homogeneous sample). The time at which the axes lengths cross does not necessarily coincide with the time that the long axis starts becoming better aligned with the direction of minimum initial compression – squares connected by dashed lines show the time at which the exchange in direction occurs.

The bottom right panels illustrate the evolution of the alignment angle in more detail. They show the angle between the mass axes and the direction of the corresponding initial deformation axis. Red, blue and black show the longest, middle and shortest axes ($\widehat{l_1\lambda_{i1}}$, $\widehat{l_2\lambda_{i2}}$ and $\widehat{l_3\lambda_{i3}}$, respectively). Thus, Figure A1 shows that halo 252 appears to rotate about its shortest axis initially; by the time the other two axes have exchanged directions, they have also reached turnaround. Thereafter, the object rotates about its longest axis, until the other two have approximately exchanged directions. The net result is that the longest and shortest axes have exchanged directions.

In contrast, the more massive halo 14 shown in Figure A2 is slightly simpler. The initial misalignment in this case was larger, but its second axis soon aligns with the intermediate axis of the initial deformation tensor, after which the object appears to rotate about this second axis until the first and third axes have exchanged directions.

Figure A3 shows another example of evolution: the initial parameters are again similar to the ones of the two previous haloes, but in this case $\lambda_3 < 0$. We see that the evolution follows a similar pattern, even if the evolution is more rapid at the beginning and the change in direction happens more than once, involving also the medium axis. However, at the end even this halo has a stronger misalignment for the shortest and longest axes, while the medium returns back towards its initial direction.

In all three cases, the misalignment angles are tens of degrees. This is in apparent contradiction with our finding in the main text that $\mu_{11} \sim 1$, which suggested perfect alignment. However, note that $\cos 20^\circ = 0.93$ which is very close to unity.

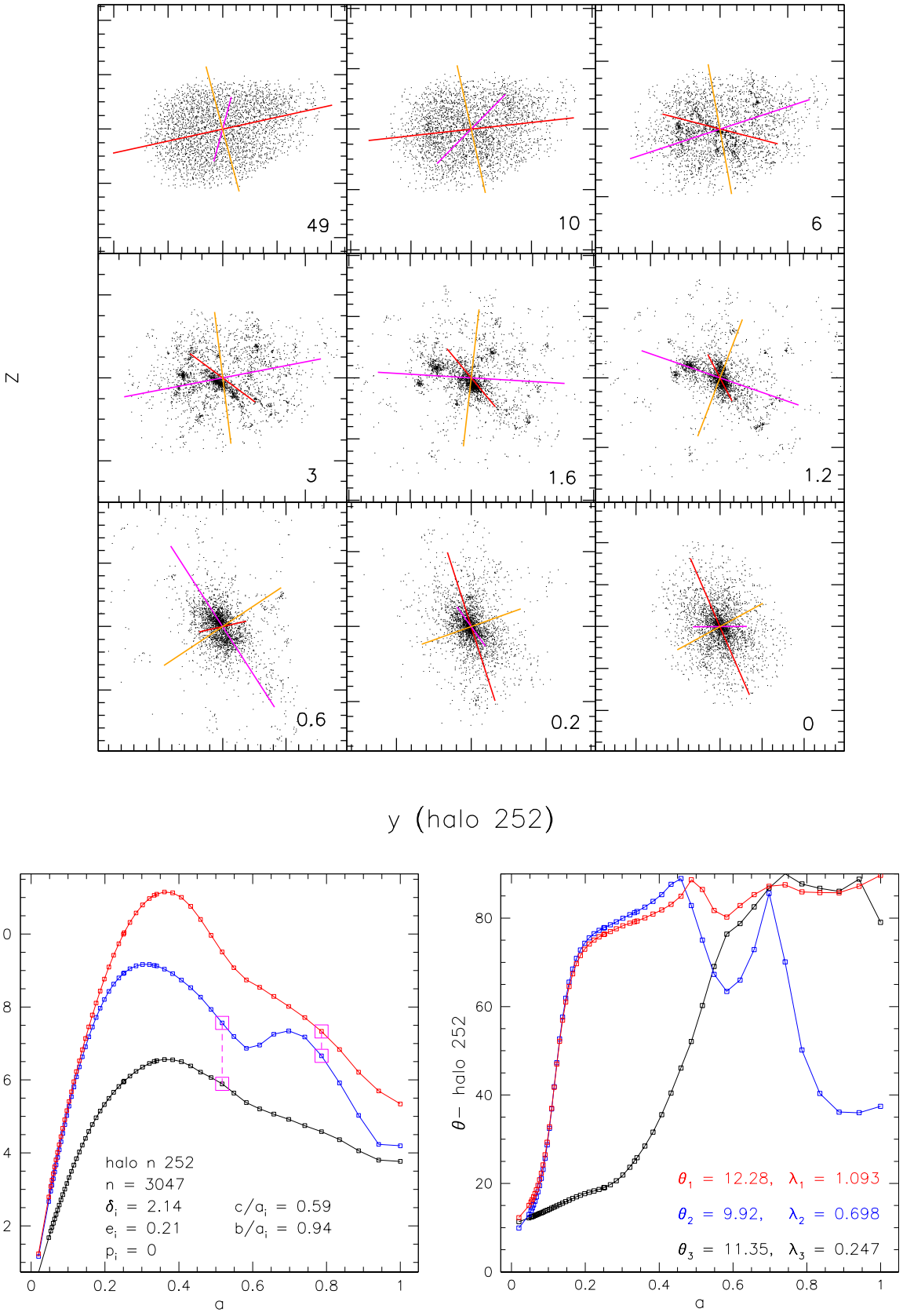


**Figure A1.** Evolution of an object of mass $M_*$. Top panels show the projected particle distribution at different redshifts (as labeled); bottom left shows the evolution of the three mass axes; bottom right shows the evolution of the angle between the mass tensor axes and the initial deformation tensor axes (the misalignment of the longest axis is shown in red, the medium in blue and the shortest in black).

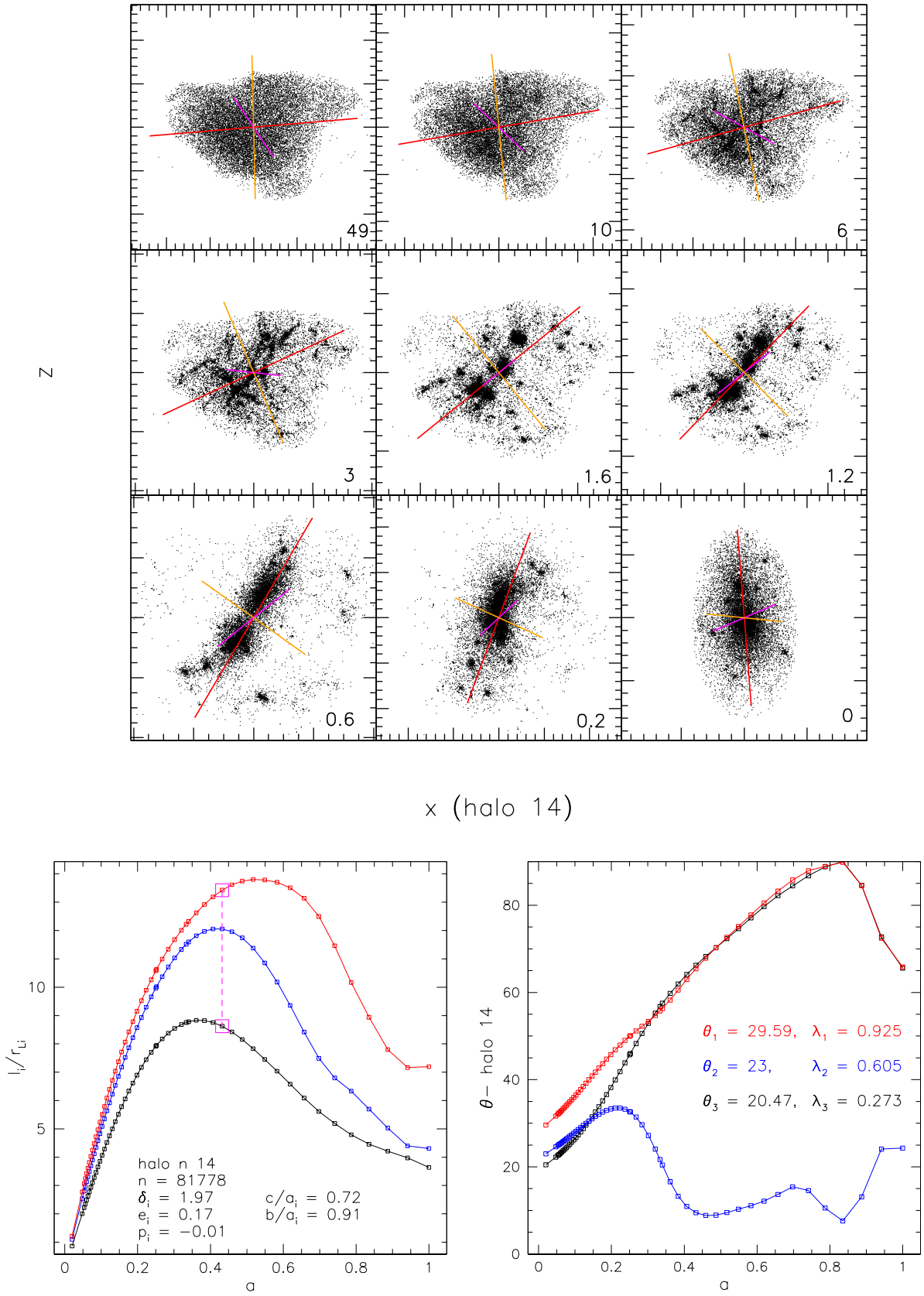


**Figure A2.** Same as previous figure, but now for an object of mass $16M*$.

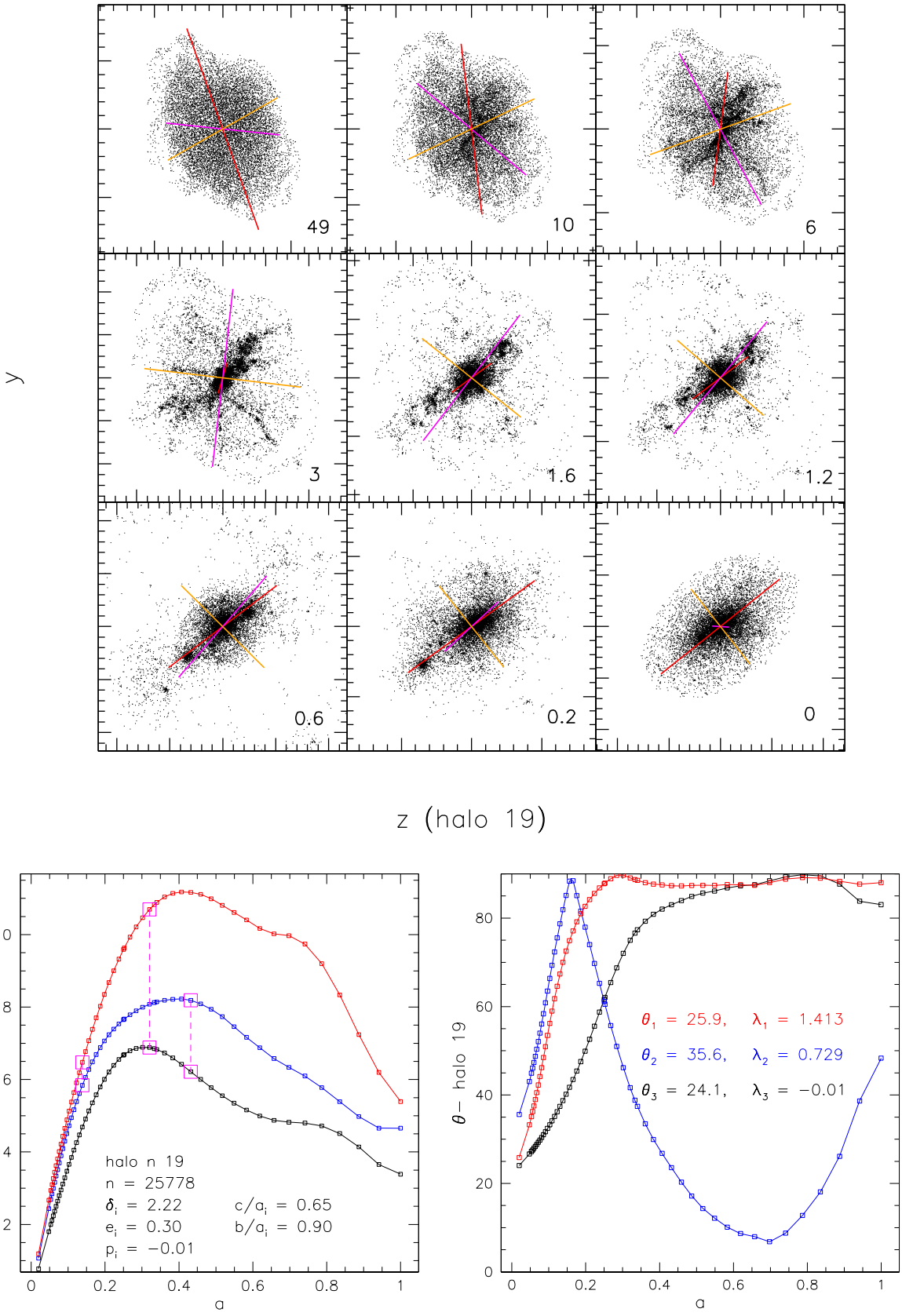


**Figure A3.** Same as previous figure, but now for an object of mass $4M*$. Notice in particular that in this case $\lambda_3 < 0$.